

Metal segregation in hierarchically structured cathode materials for high-energy lithium batteries

HPSTAR
329-2016Feng Lin¹, Dennis Nordlund², Yuyi Li¹, Matthew K. Quan¹, Lei Cheng^{1,3}, Tsu-Chien Weng^{2†}, Yijin Liu^{2*}, Huolin L. Xin^{4*} and Marca M. Doeff^{1*}

In technologically important $\text{LiNi}_{1-x-y}\text{Mn}_x\text{Co}_y\text{O}_2$ cathode materials, surface reconstruction from a layered to a rock-salt structure is commonly observed under a variety of operating conditions, particularly in Ni-rich compositions. This phenomenon contributes to poor high-voltage cycling performance, impeding attempts to improve the energy density by widening the potential window at which these electrodes operate. Here, using advanced nano-tomography and transmission electron microscopy techniques, we show that hierarchically structured $\text{LiNi}_{0.4}\text{Mn}_{0.4}\text{Co}_{0.2}\text{O}_2$ spherical particles, made by a simple spray pyrolysis method, exhibit local elemental segregation such that surfaces are Ni-poor and Mn-rich. The tailored surfaces result in superior resistance to surface reconstruction compared with those of conventional $\text{LiNi}_{0.4}\text{Mn}_{0.4}\text{Co}_{0.2}\text{O}_2$, as shown by soft X-ray absorption spectroscopy experiments. The improved high-voltage cycling behaviour exhibited by cells containing these cathodes demonstrates the importance of controlling $\text{LiNi}_{1-x-y}\text{Mn}_x\text{Co}_y\text{O}_2$ surface chemistry for successful development of high-energy lithium ion batteries.

The development of lithium ion battery technologies has spurred major breakthroughs in portable electronics, power tools, electric vehicles, and grid energy storage. In a lithium ion cell, the energy and power delivery is achieved by shuttling lithium ions between positive and negative electrodes, where the active materials undergo redox reactions using electrons from an external circuit within certain voltage windows. So far, cathode materials have received considerable attention because they are considered to be a primary determinant for increasing cell energy and power densities^{1–4}. One way to increase the practical discharge capacities of cathode materials is to increase the upper voltage limit during charge, provided that the electrolytic solution can withstand this increase in cell potential. Side reactions and thermodynamic instability of cathode materials at high voltages (high degree of lithium removal), however, have handicapped this approach. To achieve a stable cycling performance for cathode materials, it is important to maintain desirable crystal and electronic structures that allow for efficient transport of electrons and ions for the redox reactions at transition metal sites^{5,6}. Numerous studies, in particular those using electronic and structural diagnostic techniques (for example, core-level spectroscopy, electron microscopy), have shown that undesirable phase transformations occur in cathodes that can lead to failure in batteries cycled to high voltages^{7–14}. In particular, surface reconstruction (surface transition metal reduction) from a layered structure to a mixed spinel/rock-salt structure is related to the high-voltage failure of stoichiometric layered cathode materials, that is, $R\bar{3}m$ $\text{LiNi}_{1-x-y}\text{Mn}_x\text{Co}_y\text{O}_2$ (NMC; refs 7,10,11). In other cathode materials, such as lithium–manganese-rich layered NMCs

(also known as LMR-NMCs or $x\text{Li}_2\text{MnO}_3(1-x)\text{LiMO}_2$, where $M = \text{Mn, Ni, Co}$ and so on), $\text{Li}_x\text{Ni}_{0.8}\text{Co}_{0.15}\text{Al}_{0.05}\text{O}_2$ and high-voltage spinel $\text{LiNi}_{0.5}\text{Mn}_{1.5}\text{O}_4$, surface reconstruction is also a factor in the poor Coulombic efficiency, and fast capacity fading that is observed^{8,9,15–17} as well as transition metal dissolution and complexation¹⁸. Our previous density functional theory calculations indicated that, in NMC materials, the thermodynamic driving force to form rock-salt structures increases as a function of the degree of deintercalation^{11,19}. Furthermore, it has been shown that cathode–electrolyte side reactions (for example, simply by exposing NMC materials to LiPF_6 -based organic electrolytic solutions) also contribute to the surface reconstruction¹².

Partial substitution (2–4 at.%) of Ti on the Co site can improve the stability of NMC materials charged to high voltages because the rock-salt formation is delayed to higher states of charge compared with the unsubstituted NMC analogue^{19–21}. Nevertheless, capacity fading in lithium half-cells containing Ti-substituted NMCs cycled to 4.7 V is still evident¹⁹. Post-mortem analyses of these cells showed the presence of spinel or rock-salt phases on the surfaces of cycled cathode particles^{11,12}. Recently, there has been increasing interest in designing interfaces for battery materials, because controlling these interfaces can potentially enable efficient ion and electron transport^{22–25}. Forming interfaces between particles can also limit the area of contact between cathode particles and the electrolytic solution and potentially inhibit undesired side reactions^{12,26}. The cycling stability of NMC materials is also governed by the chemical composition, in particular at the surfaces^{27–29}. Therefore, the engineering of elemental distribution in NMC ensembles can also

¹Energy Storage and Distributed Resources Division, Lawrence Berkeley National Laboratory, Berkeley, California 94720, USA. ²Stanford Synchrotron Radiation Lightsource, SLAC National Accelerator Laboratory, Menlo Park, California 94025, USA. ³Department of Materials Science and Engineering, University of California, Berkeley, California 94720, USA. ⁴Center for Functional Nanomaterials, Brookhaven National Laboratory, Upton, New York 11973, USA. [†]Present address: Center for High Pressure Science & Technology Advanced Research, Shanghai 201203, China. *e-mail: liuyijin@slac.stanford.edu; hxin@bnl.gov; mmdoeff@lbl.gov

potentially improve high-voltage cycling stability. In this work, to test these hypotheses, we adopted a scalable spray pyrolysis technique^{30–33} to design hierarchically structured NMC powders consisting of large (5–20 μm) spherical particles made up of strongly interfaced nanosized primary particles in which the transition metals are selectively segregated. The resulting materials exhibit excellent resistance against surface reconstruction leading to improved high-voltage electrochemical performance. The present study sets a refined example for optimizing the surface chemistry and morphology of battery materials for vehicular and energy storage technologies.

Characterization of NMC materials

Spray pyrolysis was carried out using a home-made system^{34,35} (see Methods). The precursor was first prepared by ultrasonically spraying an aqueous solution of mixed metal nitrates through a quartz tube at 700 °C with air as the carrier gas, and this poorly crystalline powder (see Supplementary Fig. 1 for X-ray diffraction (XRD) data) was subsequently annealed at 850 °C for 6 h in a box furnace. The global chemical composition of the resulting NMC material is very close to the target composition (see Supplementary Fig. 2 for large-area energy-dispersive spectroscopy). Energy-resolved transmission X-ray microscopy^{36–38} (TXM) was used to determine the distribution of transition metals (that is, Mn, Co, Ni) in the precursor powder (Fig. 1a–e) and the final $\text{LiNi}_{0.4}\text{Mn}_{0.4}\text{Co}_{0.2}\text{O}_2$ (NMC-442) product (Fig. 1f–j). Movies of the three-dimensional (3D) elemental distribution are shown in Supplementary Videos 1 and 2. The representative slices (one voxel thickness, 32.5 nm) through the 3D volume of the hollow microspheres are shown in Fig. 1b–d, g–i. All of the transition metals are present in individual secondary particles, indicating that there was no segregation of elements at the secondary particle level. We then analysed the elemental association throughout the 3D volume by performing a correlation analysis of the absorption coefficient as a function of the X-ray energies (above and below the K-edges of all the three transition metal elements, see Methods). The Mn–Co–Ni association was only 70% for both the lithium-containing precursor powder and the annealed NMC-442 product. Ten per cent of the total voxels contain a single transition metal in the precursor (Fig. 1e), which reduced to 5% after annealing at 850 °C (Fig. 1j). This observation indicates the migration of transition metals during thermal annealing.

Direct visualization was achieved by colour mapping individual elemental associations in three dimensions, as shown in Fig. 2. The associated movie of the 3D chemical associations is shown in Supplementary Video 3. A large number of nanodomains showed significant deviation from the global NMC-442 composition in both the as-made precursor and the annealed NMC particles. There are fewer three-element domains on the surfaces of the annealed NMC particles compared with the precursor particles (compare Fig. 2a and c). The interior elemental associations were visualized by slicing through the particles at different depths and are shown in Fig. 2b, d. Although the bulks of these particles also deviated from the global NMC-442 composition in parts, there are more three-element domains than on the surfaces for both types of sample. These 3D and 2D elemental association maps clearly show that there is segregation of transition metals throughout the hierarchically structured materials, particularly in the annealed powder and at the surfaces. Metal segregation at a similar nanometre scale was also observed previously in lithium–manganese-rich layered materials³⁹.

The NMC-442 materials are 5–20 μm microspheres that consist of 50–200 nm primary particles (Fig. 3a, b), which allows for shorter lithium diffusion distances^{31,40}. Although the 3D Ni–Mn–Co association was only 70% (Figs 1 and 2), the resulting NMC-442 material exhibits the expected $R\bar{3}m$ layered structure

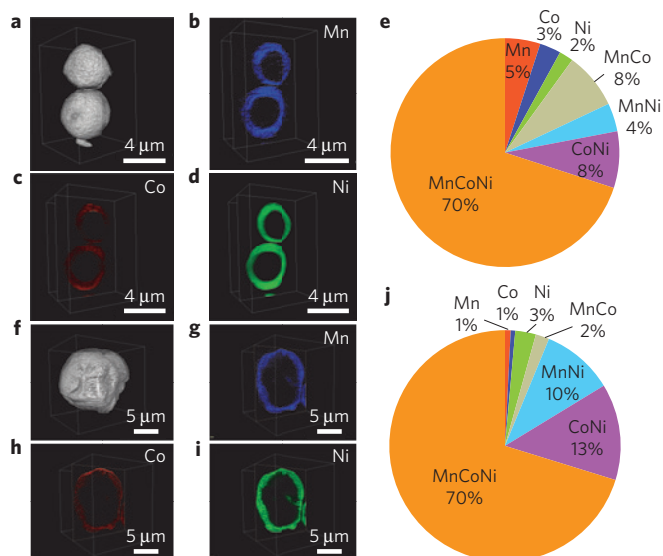


Figure 1 | Elemental mapping and association calculation using transmission X-ray tomography. **a–i**, 3D elemental distribution of selected NMC particles collected directly after spray pyrolysis (**a–d**) and after subsequent annealing at 850 °C (**f–i**). Single-energy tomography provides the 3D morphology of the particles (**a, f**), multi-energy tomography data with elemental sensitivity, visualized by slicing through the centre of the particles, with blue, red and green representing Mn, Co and Ni, respectively (**b–d, g–i**), and the relative concentrations of 3D elemental associations calculated by using absorption correlation tomography (**e, j**) for NMC particles collected directly after spray pyrolysis (**a–d**) and after subsequent annealing at 850 °C (**f–i**). Movies of 3D elemental distributions are shown in Supplementary Videos 1 and 2.

with approximately 5.6% Li–Ni cation intermixing estimated from the Rietveld refinement (Fig. 3c) using the standard NMC-442 $R\bar{3}m$ model, with no evidence of impurity phases in the XRD pattern. In addition, the refined lattice parameters ($a = b = 2.8708 \text{ \AA}$, $c = 14.2518 \text{ \AA}$) are close to those previously reported for NMC materials^{41,42}. High-resolution scanning electron microscopy (SEM) imaging shows the primary particles in close contact with one another (Fig. 3d). The intergranular region enclosed by the rectangle in Fig. 3d was further studied by aberration-corrected angular dark-field scanning transmission electron microscopy (ADF-STEM) and electron energy loss spectroscopy (EELS). Figure 3e shows the ADF-STEM Z-contrast image of the selected area in Fig. 3d, where the adjacent particles are perfectly distinguished by the distinct thickness contrasts. In the brighter particle (top left) two domains that are π out of phase are projected in this image. The presence of Mn^{4+} and strong transition metal 3d–oxygen 2p (TM3d–O2p) hybridization states is indicative of a pristine $R\bar{3}m$ layered NMC; in contrast, in the rock-salt structure commonly observed when surface reconstruction occurs, the transition metals are divalent (for example, Mn^{2+}) and the hybridization state is much weaker^{9,12,15}. EELS scanning profile was performed across the intergranular boundary along the indicated direction in the selected area (Fig. 3e) and spectra were recorded every 90 \AA^2 (Fig. 3f). There were essentially no changes in either O K-edge X-ray absorption spectroscopy (XAS) or Mn L-edge EELS spectra along the scanning pathway. The high TM3d–O2p hybridization intensity is consistent with what is typically reported for pristine $R\bar{3}m$ layered cathode materials^{9,12,15}. Therefore, the above characterization at complementary length scales has clearly demonstrated that the resulting materials have the expected $R\bar{3}m$ layered structure. Furthermore, the particle–particle boundary has extremely good coherence, and the bonding environment of

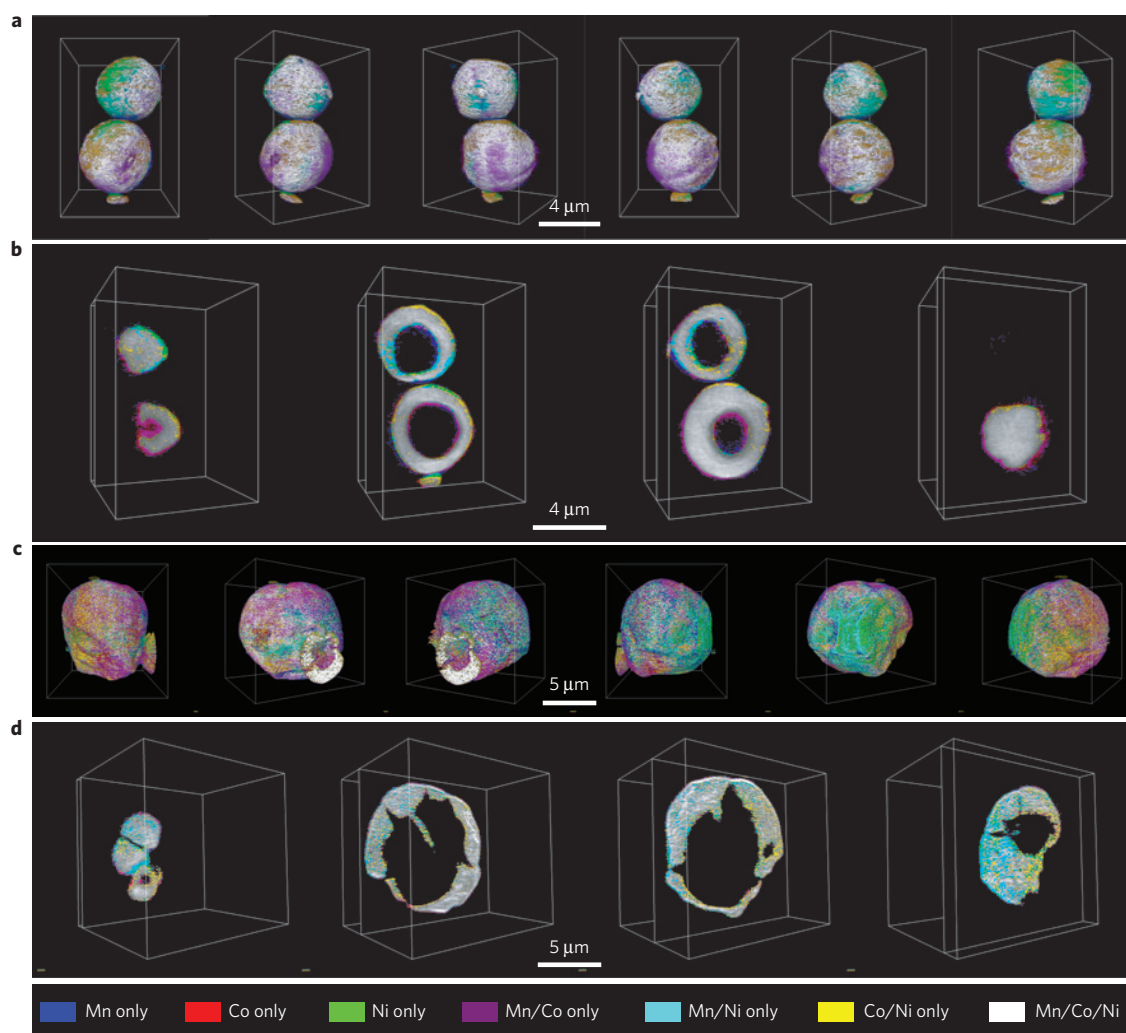


Figure 2 | 3D elemental association maps generated using transmission X-ray tomography. a–d. Elemental association maps of the as-made NMC precursor after spray pyrolysis (**a,b**) and the powder after annealing at 850 °C (**c,d**). **a,c**, 3D rendering of the elemental associations viewing the particles at different angles, where the visualization is enhanced in Supplementary Video 3 for the powder after annealing at 850 °C. **b,d**, 2D slices of the elemental associations cut through at different depths of the imaged particles. The colours representing the elemental associations are shown at the bottom.

cations is not disrupted at the intergranular boundary, as is clearly demonstrated by the STEM–EELS result.

The elemental distribution at the atomic scale also seems to be inhomogeneous. The EELS spectra were normalized using the Mn L-edge and the evolution of the Co and Ni L-edge intensities was monitored (Fig. 4). From the stacked spectra, it is apparent that these do not remain constant along the scanning pathway. To quantify this, we integrated the area of the Ni L₃-edge for each measured area and found that the Ni L₃-integrated area fluctuated along the scanning area (Fig. 4b). These observations show that the inhomogeneities are on both an atomic scale (Fig. 4) and a nanometric scale (Figs 1 and 2).

Electrochemical measurements of NMC materials

The electrochemical performance of the spray-pyrolysed and annealed NMC-442 was characterized in lithium half-cells. First-cycle Coulombic inefficiencies as high as 20% are characteristic of cells containing NMC materials and are observed even after partial charging to voltage limits well below the thermodynamic stability limit of the electrolytic solution^{20,43}. The cells containing the spray-pyrolysed NMC electrodes exhibited much lower first-cycle Coulombic inefficiencies than what is typical for unsubstituted NMCs (a maximum of 11.4% when cycled to 4.7 V, Fig. 5a)

and less charge–discharge polarization than those containing co-precipitated Ti-substituted NMC and combustion-synthesized NMC electrodes (Supplementary Fig. 3). The improved efficiencies and reduced polarization result in higher capacities than usual on the subsequent discharge, particularly for cells cycled to higher voltages (for example, 228 mAh g⁻¹ between 2.0 and 4.7 V, compared with 200 mAh g⁻¹ for a reference material made by combustion synthesis). In fact, the results are similar to those previously reported for Ti-substituted NMC442 materials, which exhibited improved efficiencies and higher discharge capacities compared with those of unsubstituted NMCs made by combustion synthesis during high-voltage cycling^{20,21}. Although capacity fading is still observed for cells containing the spray-pyrolysed NMC cycled to 4.7 V, retention is better than that of the reference material, even though more capacity is cycled (Fig. 5b,c), namely, there is a higher degree of lithium intercalation and deintercalation. When the cutoff voltages are decreased to 4.5 V and 4.3 V, the cycling stability of the NMC442 material is significantly improved (Fig. 5b,c), although the practical discharge capacities are lower. The effect of changing the lower discharge voltage (Fig. 5d) is much less than that of the upper voltage, both in terms of the practical capacity and the capacity retention. The differences between the spray-pyrolysed and reference samples under this short

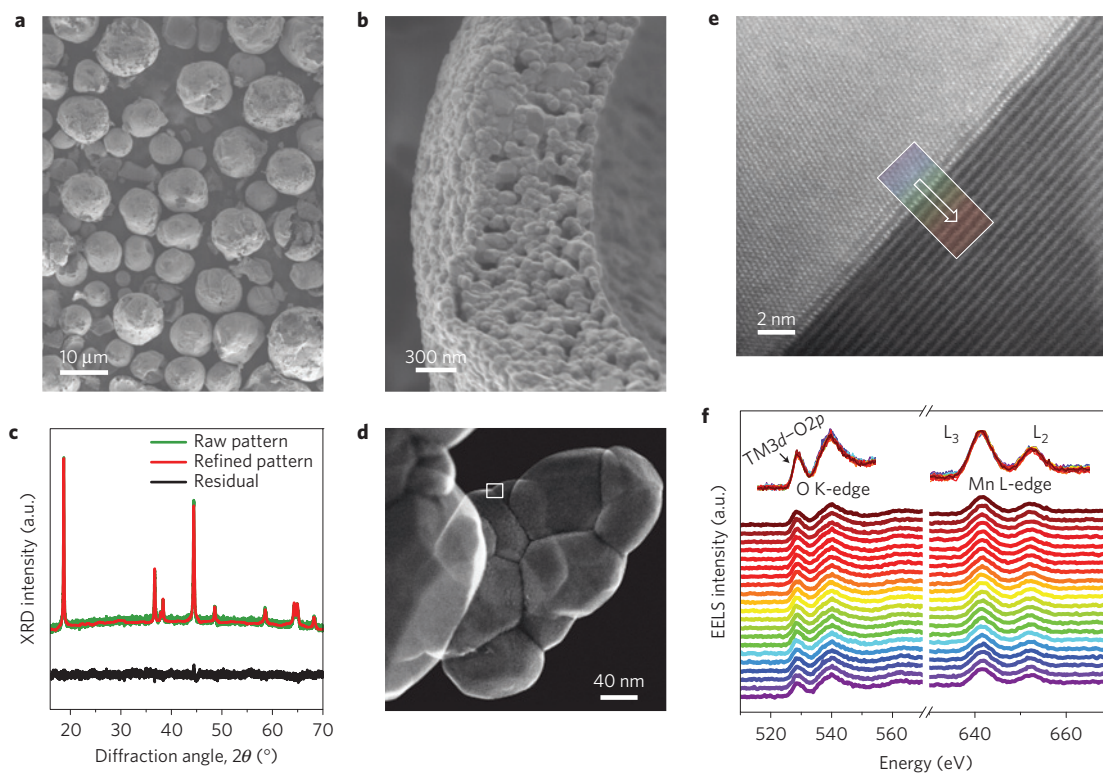


Figure 3 | Characterization of the NMC-442 materials synthesized by spray pyrolysis. **a, b,** SEM at different magnifications. **c,** XRD and Rietveld refinement. **d–f,** SEM-STEM-EELS, where a selected particle–particle interface marked in **d** was used for ADF-STEM imaging (**e**) and EELS O K-edge and Mn L-edge measurements (**f**). In the brighter particle (top left) in **e**, two domains that are π out of phase are projected in this image.

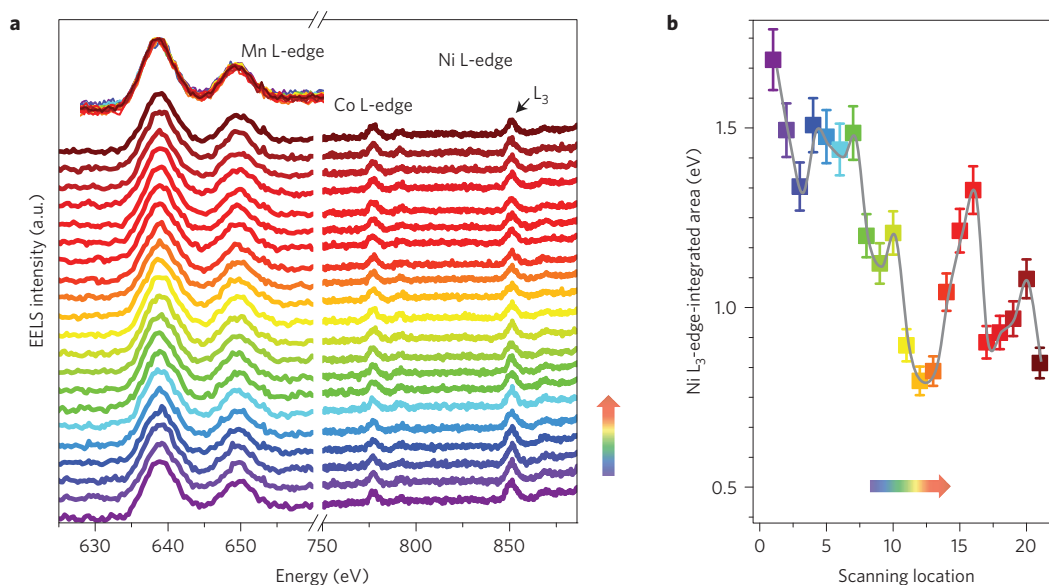


Figure 4 | Electronic and compositional characterization using EELS. **a,** Transition metal L-edge EELS spectra along the scanning pathway shown in Fig. 3e, where the spectra were normalized using the Mn L-edge. The normalized spectra were overlapped on the top of the stacked spectra, demonstrating the identical peak characteristics for all of the Mn L-edge spectra. **b,** The Ni L_3 -integrated areas calculated after the Mn L-edge normalization. The error bars are based on multiple peak area calculations and the line is to assist visualization. The coloured arrows in the figure represent the scanning direction corresponding to the one in Fig. 3e.

cycling regime to high potentials are primarily due to the effects of the cathode surface chemistries on the surface reconstruction phenomena, rather than dendrite formation and side reactions due to electrolytic oxidation, which influence behaviour during prolonged cycling.

Investigation of structural stability and surface chemistry

Surface reconstruction from a layered structure to mixed spinel/rock-salt structures, involving the loss of lithium and oxygen and the reduction of transition metals^{7,11} contributes, to the failure of NMC materials cycled to high voltages. As the fraction

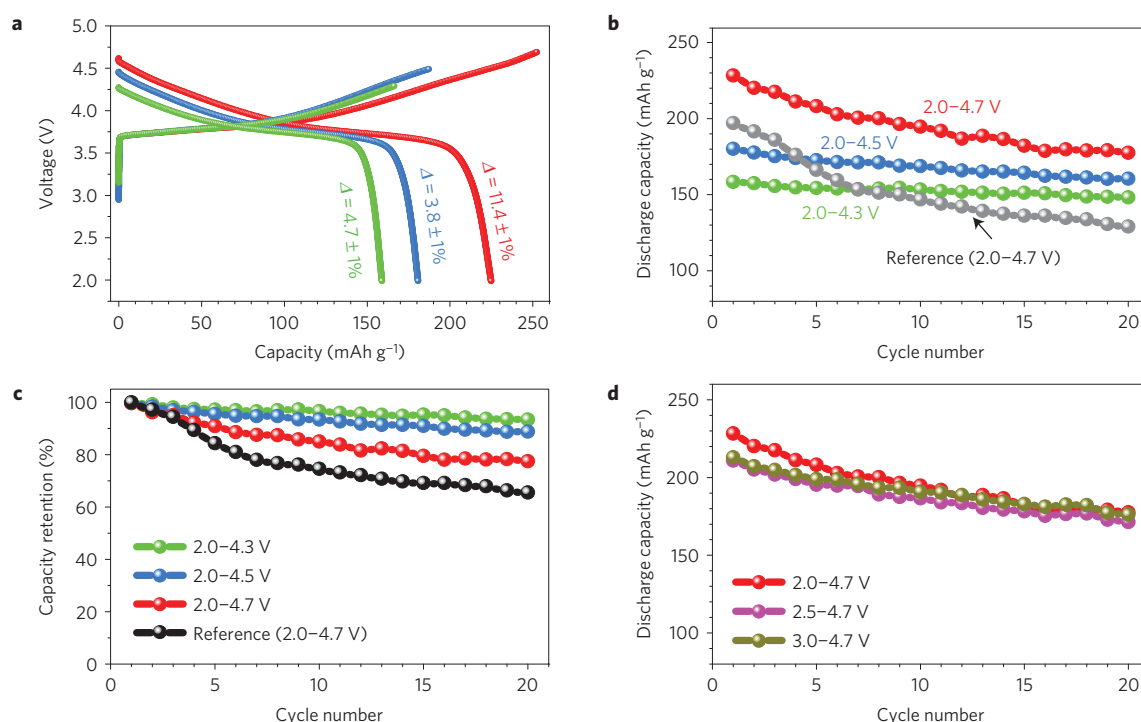


Figure 5 | Battery cycling performance of lithium half-cells containing the NMC-442 materials. **a**, First charge–discharge cycles between various voltage cutoff windows with percentage Coulombic inefficiencies indicated. Red, blue and green lines represent voltage limits of 2.0–4.7 V, 2.0–4.5 V and 2.0–4.3 V, respectively. These cells were cycled at approximately similar rates. **b**, Discharge capacities as a function of cycle numbers during the galvanostatic cycling, with reference data taken from ref. 21 on an NMC-442 material prepared by a glycine–nitrate combustion method and cycled between 2.0–4.7 V. **c**, Discharge capacity retention at various cutoff voltages during 20 cycles. **d**, Discharge capacity as functions of cycle number and cutoff voltages. All cells were cycled at approximately $C/20$ and an extra amount of electrolyte was added in coin cells to isolate the effects of electrolyte oxidation (for example, electrolyte deficiency).

of surface reconstruction is trivial compared with the bulk in NMC particles, bulk-sensitive techniques, such as extended X-ray absorption fine structure, XRD and hard X-ray absorption near-edge spectroscopy, are unlikely to reveal much information about the structural transformation. We have previously established a statistically viable protocol based on high-throughput synchrotron soft X-ray absorption spectroscopy^{11,12}, where signals from approximately 10^7 primary particles (estimated using X-ray beam size and primary particle size, 99.97% representing the mean of an infinite ensemble) can be collected at one time. Depending on the mode, different sample depths can be accessed; in the total electron yield (TEY) mode used for the experiments in Fig. 6, the probing depth is about 5–10 nm. Surface reconstruction has also previously been observed on particles removed from cycled cells through STEM–EELS experiments, verifying the soft XAS results¹¹. The measurement was performed on composite electrodes containing NMC-442 materials in the discharged state after 20 cycles. The oxidation states of Mn and Co can be used to track the formation of reduced species on particle surfaces for NMCs in the discharged state, consistent with formation of a rock-salt phase. However, Ni is divalent in both the discharged NMC-442 layered structure and the rock-salt phase and thus cannot be used to track surface reconstruction. The transition metal L-edge corresponds to the dipole-allowed transitions from $2p$ to $3d$ states, including $2p_{3/2}$ (L_3 -edge) and $2p_{1/2}$ (L_2 -edge) spin–orbit final states^{44–46}. There was no difference between spray-pyrolysed and co-precipitated NMC-442 materials in the pristine states and the results are consistent with Mn in the tetravalent state and Co in the trivalent state as expected (blue spectra in Fig. 6a,b)¹¹. However, low-energy shoulders of Mn L_3 - and Co L_3 -edges appeared and grew after extended charge–discharge cycles to 4.7 V, indicating

an evolution of transition metal $3d$ bands to higher occupancies consistent with reduced oxidation states. The reduction of Mn and Co was significantly less severe in the cycled spray-pyrolysed NMC materials compared with that in the co-precipitated ones, even though more capacity was cycled in the former. This indicates that the spray-pyrolysed NMC had superior resistance against surface reconstruction (reduction of surface transition metals), which can explain the enhanced high-voltage cycling stability (Fig. 5). The cycling stability of NMC materials is clearly affected by the nanoscale transition metal distribution at the surface^{27,28}. It is known that nickel-rich cathode materials have a tendency to lose oxygen and to form surface reduced layers, because the unpaired e_{2g} electrons make the high-valency nickel ions (for example, Ni^{3+}) thermodynamically unstable⁴⁷, according to crystal-field theory. To counteract this tendency, compositionally graded cathodes with manganese-rich surfaces have been designed to improve cell safety and cycling characteristics^{27,28}. The depth-dependent elemental distribution (calculated using TXM data, Fig. 6c) shows that the surfaces (including internal and external surfaces of the subject NMC hollow microspheres) are poorer in nickel and cobalt content and richer in manganese relative to the global NMC-442 composition. The end result of the fortuitous metal segregation that occurs during processing of the NMC-442 microspheres is less surface reconstruction, leading to improved high-voltage cycling performance. In contrast, in the co-precipitated NMC-442 material (Fig. 7), most voxels (more than 90%, see the pie chart in Fig. 7b) in the particle have all three transition metals, and Co is absent in some of the isolated sub-regions (shown in cyan in Fig. 7a), in a random distribution pattern, accounting for only about 7.6% of the total volume. The rest of the elemental associations occupy less than 1% of the total volume and are, thus, not visible in either Fig. 7a or b.

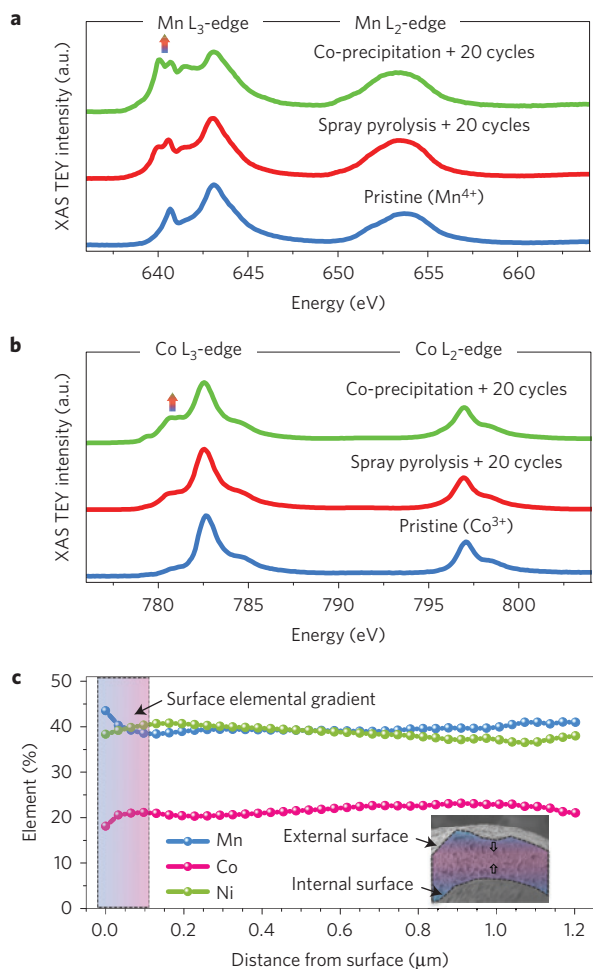


Figure 6 | Surface chemistry of NMC materials before and after electrochemical cycling. **a,b**, XAS spectra of Mn L-edge (**a**) and Co L-edge (**b**) of NMCs in the pristine state (blue) and after 20 charge-discharge cycles to 4.7 V versus Li/Li⁺ (red and green), stopped in the discharged state. Transition metal L-edges are divided into L₃ and L₂ features located at lower and higher energy regions of the spectra, respectively. The small arrows point to the Mn and Co L_{3,low} edges, which increase in magnitude in cycled electrodes compared with pristine ones, indicating that the oxidation states of metals near the surfaces are lower in the former compared with the latter. The co-precipitation data are used with permission from ref. 11. **c**, Elemental distribution as a function of the distance from microsphere surface calculated using the TXM data, and the elemental distribution at the surface region is highlighted using the blue-magenta shadow. The distance from surface was calculated from both the internal and external surfaces of the hollow shell, as schematically shown in the inset.

The depth profile of the elemental concentrations of the studied particle (shown in Fig. 7c) also indicates that the co-precipitated particle is relatively more homogeneous than the spray-pyrolysed one, especially at the secondary particle's surface layer. Therefore, the direct performance and characterization comparisons suggest that the selective metal segregation can indeed deliver higher electrochemical performance.

Conclusions

We have synthesized hierarchically structured LiNi_{0.4}Mn_{0.4}Co_{0.2}O₂ (NMC-442) cathode materials consisting of nanoparticles agglomerated into larger spherical secondary particles. The materials have the expected *R3m* layered structure with a global composition close

to the nominal composition, but showed chemical inhomogeneities on both atomic and nanometric length scales. The 3D structural and elemental mapping suggested that the NMC-442 material consists of nanodomains that deviate from the global NMC-442 composition, in particular at the surface regions of the secondary particles, where nickel is depleted. The electrochemical performance measured in lithium half-cells showed superior first-cycle Coulombic efficiencies, higher practical discharge capacities and better capacity retention compared with the NMC-442 materials prepared by glycine-nitrate combustion and co-precipitation methods. Mn L-edge and Co L-edge XAS showed that the present NMC-442 material exhibited superior resistance against surface reconstruction because of the nickel-depleted and manganese-rich surfaces, accounting for the better electrochemical properties. This study indicates that engineering the nanoscale elemental distribution in NMCs may be a fruitful path forward for designing higher energy densities in lithium batteries. From the technological point of view, it is very desirable for the design of energy materials if microscopic techniques with 3D chemical sensitivity at relevant length scales can be applied to investigate the *in operando* behaviour of materials in practical environments. The combination of state-of-the-art X-ray and electron microscopy is an excellent candidate for this. However, we would also point out that it is critical to actively develop new methodologies for reducing the total amount of dose associated with the measurement, to mitigate possible radiation damage.

Methods

Materials synthesis. The NMC materials were synthesized by spray pyrolysis followed by thermal annealing in a box furnace. The spray pyrolysis set-up has been discussed previously^{34,35}. A 0.8 M (total transition metal ions) aqueous precursor solution containing metal nitrates with molar ratios of lithium, nickel, manganese and cobalt equal to 10.5:4:4:2 was prepared. The solution was transferred to a syringe pump and delivered to an atomizer nozzle (Sonozap Model 120K50ST, 120 kHz) at a flow rate of 0.5 ml min⁻¹ to generate microdroplets, which were then carried through a preheated quartz tube (700 °C) by air at a flow rate of 20 SCFH. The precursor microdroplets decomposed to form a powder and were collected at the end of the tube. This powder was then annealed in air for 6 h with heating and cooling rates of 2 °C min⁻¹. A co-precipitation procedure described previously¹⁰⁻¹² was used to produce the sample shown in Fig. 7.

Electrode preparation and electrochemical measurement. Composite electrodes were prepared with 84 wt% active material, 8 wt% polyvinylidene fluoride (Kureha Chemical Ind.), 4 wt% acetylene carbon black (Denka, 50% compressed) and 4 wt% SFG-6 synthetic graphite (Timcal, Graphites and Technologies) in *N*-methyl-2-pyrrolidone and cast onto carbon-coated aluminium current collectors (Exopack Advanced Coatings) with typical active material loadings of 2.0–2.5 mg cm⁻². 2032-type coin cells were assembled in an argon-filled glove box using the composite electrode as the positive electrode and Li metal as the negative electrode. A Celgard 2400 separator and 1 M LiPF₆ electrolyte solution in 1:1 v/v ethylene carbonate/diethyl carbonate (EC-DEC, Novolyte Technologies) were used in the coin cells. Battery testing was performed on a computer-controlled VMP3 potentiostat/galvanostat (BioLogic). Galvanostatic cycling was performed at approximately C/20, where 1C was defined as fully charging a cathode in 1 h, corresponding to a specific current density of 280 mA g⁻¹. Each measurement was repeated to ensure the reproducibility of the electrochemical data. The electrodes were removed from the coin cells, rinsed with dimethyl carbonate and dried in an argon-filled glove box for further study. The electrodes were sealed under argon and then transferred to the synchrotron beamline using a home-made system to prevent air/moisture exposure. The samples were loaded into the vacuum chamber under Ar protection.

Materials characterization. X-ray diffraction on powder samples was performed on a Bruker D2 Phaser diffractometer using Cu K α radiation. Scanning electron microscopy was performed on a JEOL JSM-7000F with a Thermo Scientific energy-dispersive X-ray spectroscopy detector. X-ray absorption spectroscopy measurements were performed on the 31-pole wiggler beamline 10-1 at Stanford Synchrotron Radiation Lightsources (SSRL) using a ring current of 350 mA and a 1,000 l mm⁻¹ spherical grating monochromator with 20 μ m entrance and exit slits, providing $\sim 10^{11}$ ph s⁻¹ at 0.2 eV resolution in a 1 mm² beam spot. During the measurements, all battery electrode samples were attached to an aluminium sample holder using conductive carbon tape (X-ray beam probing the top surface

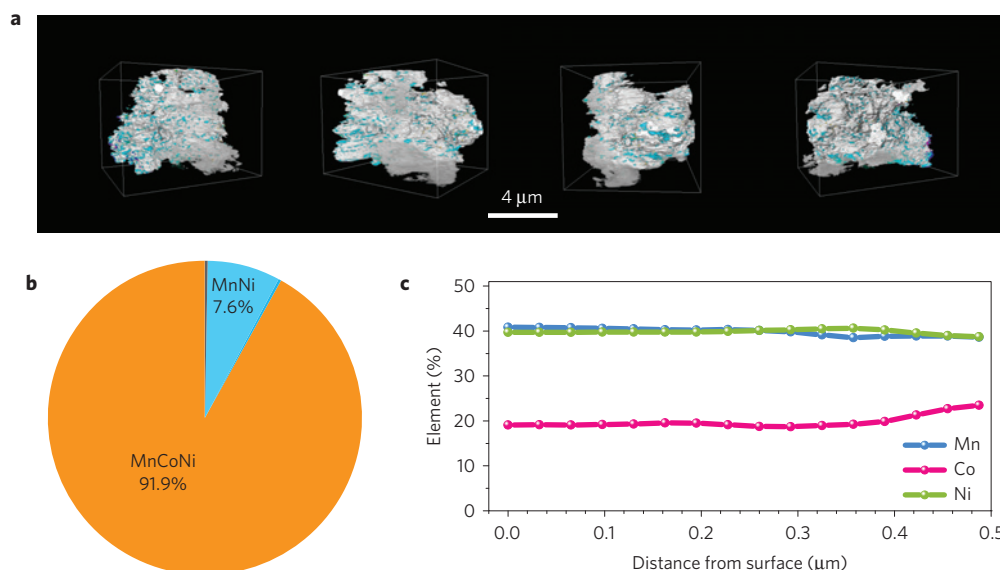


Figure 7 | 3D elemental association mapping and elemental distribution of co-precipitated NMC particles. **a**, Elemental association maps of a particle selected from the co-precipitated sample, where the cyan colour represents the regions where Co was not observed. **b**, The relative concentrations of 3D elemental associations calculated by using absorption correlation tomography; elemental associations other than MnCoNi and MnNi were all below 1% such that they are negligible in the pie chart. **c**, Elemental distribution as a function of the distance from the secondary particle surface calculated using the TXM data, in direct comparison with Fig. 6c.

of the composite electrodes). Data were acquired under ultrahigh vacuum (10^{-9} torr) in a single load at room temperature using the total electron yield (TEY) mode. The sample drain current was collected for TEY. All spectra were normalized by the current from freshly evaporated gold on a fine grid positioned upstream of the main chamber. The transmission X-ray microscopy was performed at beamline 6-2c of the SSRL. The details of the experimental set-up can be found in a previous publication⁴⁸. The samples were loaded in quartz capillaries enabling full rotation from -90° to 90° with an angular step size of 1° . Slow and steady helium flow was applied to the samples to reduce the radiation-induced heat load on the sample in the tomography scans. X-ray nano-tomography was performed at 6 different energies (6,530 eV, 6,550 eV, 7,700 eV, 7,720 eV, 8,324 eV and 8,344 eV) above and below the K-edges of the three transition metal elements (Mn, Co, and Ni) to resolve the elemental distribution. The tomographic reconstruction, which results in an effective 3D voxel size of $32.5 \times 32.5 \times 32.5$ nm³ (spatial resolution), and the analysis of the elemental association³⁶ were performed using an in-house-developed software package known as TXM-Wizard⁴⁹. A Cs-corrected cold field emission dedicated scanning transmission electron microscope operated at 200 keV was used for annular dark-field STEM imaging and spatially resolved electron energy loss spectroscopy.

Received 11 June 2015; accepted 22 October 2015;
published 11 January 2016

References

- Whittingham, M. S. Lithium batteries and cathode materials. *Chem. Rev.* **104**, 4271–4302 (2004).
- Whittingham, M. S. Ultimate limits to intercalation reactions for lithium batteries. *Chem. Rev.* **114**, 11414–11443 (2014).
- Doeff, M. M. *Batteries: Overview of Battery Cathodes* 709–739 (Springer Encyclopedia of Sustainability Science and Technology Springer Science + Business Media, LLC, 2012).
- Xu, X., Lee, S., Jeong, S., Kim, Y. & Cho, J. Recent progress on nanostructured 4V cathode materials for Li-ion batteries for mobile electronics. *Mater. Today* **16**, 487–495 (December, 2013).
- Hwang, B. J., Tsai, Y. W., Carlier, D. & Ceder, G. A combined computational/experimental study on $\text{LiNi}_{1/3}\text{Co}_{1/3}\text{Mn}_{1/3}\text{O}_2$. *Chem. Mater.* **15**, 3676–3682 (2003).
- Islam, M. S. & Fisher, C. A. J. Lithium and sodium battery cathode materials: Computational insights into voltage, diffusion and nanostructural properties. *Chem. Soc. Rev.* **43**, 185–204 (2014).
- Jung, S.-K. *et al.* Understanding the degradation mechanisms of $\text{LiNi}_{0.5}\text{Co}_{0.2}\text{Mn}_{0.3}\text{O}_2$ cathode material in lithium ion batteries. *Adv. Energy Mater.* **4**, 1300787–1300794 (2013).
- Xu, B., Fell, C. R., Chi, M. & Meng, Y. S. Identifying surface structural changes in layered Li-excess nickel manganese oxides in high voltage lithium ion batteries: A joint experimental and theoretical study. *Energy Environ. Sci.* **4**, 2223–2233 (2011).
- Hwang, S. *et al.* Investigation of changes in the surface structure of $\text{Li}_x\text{Ni}_{0.8}\text{Co}_{0.15}\text{Al}_{0.05}\text{O}_2$ cathode materials induced by the initial charge. *Chem. Mater.* **26**, 1084–1092 (2014).
- Lin, F. *et al.* Influence of synthesis conditions on the surface passivation and electrochemical behavior of layered cathode materials. *J. Mater. Chem. A* **2**, 19833–19840 (2014).
- Lin, F. *et al.* Surface reconstruction and chemical evolution of stoichiometric layered cathode materials for lithium-ion batteries. *Nature Commun.* **5**, 3529 (2014).
- Lin, F. *et al.* Profiling the nanoscale gradient in stoichiometric layered cathode particles for lithium-ion batteries. *Energy Environ. Sci.* **7**, 3077–3085 (2014).
- Yang, F. *et al.* Nanoscale morphological and chemical changes of high voltage lithium-manganese rich NMC composite cathodes with cycling. *Nano Lett.* **14**, 4334–4341 (2014).
- Abraham, D. P. *et al.* Microscopy and spectroscopy of lithium nickel oxide-based particles used in high power lithium-ion cells. *J. Electrochem. Soc.* **150**, A1450–A1456 (2003).
- Zheng, J. *et al.* Corrosion/fragmentation of layered composite cathode and related capacity/voltage fading during cycling process. *Nano Lett.* **13**, 3824–3830 (2013).
- Lin, M. *et al.* Insight into the atomic structure of high-voltage spinel $\text{LiNi}_{0.5}\text{Mn}_{1.5}\text{O}_4$ cathode material in the first cycle. *Chem. Mater.* **27**, 292–303 (2015).
- Qiao, R. *et al.* Direct evidence of gradient Mn(II) evolution at charged states in $\text{LiNi}_{0.5}\text{Mn}_{1.5}\text{O}_4$ electrodes with capacity fading. *J. Power Sources* **273**, 1120–1126 (2015).
- Jarry, A. *et al.* The formation mechanism of fluorescent metal complexes at the $\text{Li}_{(x)}\text{Ni}_{(0.5)}\text{Mn}_{(1.5)}\text{O}_{(4-\delta)}$ /carbonate ester electrolyte interface. *J. Am. Chem. Soc.* **137**, 3533–3539 (2015).
- Markus, I. M., Lin, F., Kam, K. C., Asta, M. & Doeff, M. M. Computational and experimental investigation of Ti substitution in $\text{Li}_1(\text{Ni}_x\text{Mn}_x\text{Co}_{1-2x-y}\text{Ti}_y)\text{O}_2$ for lithium ion batteries. *J. Phys. Chem. Lett.* **5**, 3649–3655 (2014).
- Kam, K. C. & Doeff, M. M. Alivalent titanium substitution in layered mixed Li Ni–Mn–Co oxides for lithium battery applications. *J. Mater. Chem.* **21**, 9991–9993 (2011).
- Kam, K. C., Mehta, A., Heron, J. T. & Doeff, M. M. Electrochemical and physical properties of Ti-substituted layered nickel manganese cobalt oxide (NMC) cathode materials. *J. Electrochem. Soc.* **159**, A1383–A1392 (2012).
- Maier, J. Nanoionics: Ion transport and electrochemical storage in confined systems. *Nature Mater.* **4**, 805–815 (2005).

23. Nie, A. *et al.* Twin boundary-assisted lithium ion transport. *Nano Lett.* **15**, 610–615 (2015).
24. Cheng, L. *et al.* The origin of high electrolyte–electrode interfacial resistances in lithium cells containing garnet type solid electrolytes. *Phys. Chem. Chem. Phys.* **16**, 18294–18300 (2014).
25. Cheng, L. *et al.* Effect of surface microstructure on electrochemical performance of garnet solid electrolytes. *ACS Appl. Mater. Interfaces* **7**, 2073–2081 (2015).
26. Belharouak, I., Lu, W., Vissers, D. & Amine, K. Safety characteristics of $\text{Li}(\text{Ni}_{0.8}\text{Co}_{0.15}\text{Al}_{0.05})\text{O}_2$ and $\text{Li}(\text{Ni}_{1/3}\text{Co}_{1/3}\text{Mn}_{1/3})\text{O}_2$. *Electrochem. Commun.* **8**, 329–335 (2006).
27. Sun, Y.-K. *et al.* High-energy cathode material for long-life and safe lithium batteries. *Nature Mater.* **8**, 320–324 (2009).
28. Sun, Y.-K. *et al.* Nanostructured high-energy cathode materials for advanced lithium batteries. *Nature Mater.* **11**, 942–947 (2012).
29. Cho, Y., Oh, P. & Cho, J. A new type of protective surface layer for high-capacity Ni-based cathode materials: Nanoscaled surface pillaring layer. *Nano Lett.* **13**, 1145–1152 (2013).
30. Jung, D. S., Ko, Y. N., Kang, Y. C. & Park, S. B. Recent progress in electrode materials produced by spray pyrolysis for next-generation lithium ion batteries. *Adv. Powder Technol.* **25**, 18–31 (2014).
31. Zhang, X. & Axelbaum, R. L. Spray pyrolysis synthesis of mesoporous lithium–nickel–manganese-oxides for high energy Li-ion batteries. *J. Electrochem. Soc.* **159**, A834–A842 (2012).
32. Jung, D. S. *et al.* Hierarchical porous carbon by ultrasonic spray pyrolysis yields stable cycling in lithium–sulfur battery. *Nano Lett.* **14**, 4418–4425 (2014).
33. Bang, J. H., Didenko, Y. T., Helmich, R. J. & Suslick, K. S. Nanostructured materials through ultrasonic spray pyrolysis. *Mater. Matters* **7**, 19–25 (2012).
34. Liu, J., Conry, T. E., Song, X., Doeff, M. M. & Richardson, T. J. Nanoporous spherical LiFePO_4 for high performance cathodes. *Energy Environ. Sci.* **4**, 885–888 (2011).
35. Liu, J. *et al.* Spherical nanoporous LiCoPO_4/C composites as high performance cathode materials for rechargeable lithium-ion batteries. *J. Mater. Chem.* **21**, 9984–9987 (2011).
36. Kao, T. L. *et al.* Nanoscale elemental sensitivity study of $\text{Nd}_2\text{Fe}_{14}\text{B}$ using absorption correlation tomography. *Microsc. Res. Tech.* **76**, 1112–1117 (2013).
37. Meirer, F. *et al.* Three-dimensional imaging of chemical phase transformations at the nanoscale with full-field transmission X-ray microscopy. *J. Synchrotron Radiat.* **18**, 773–781 (2011).
38. Wang, J., Chen-Wiegart, Y. K. & Wang, J. In operando tracking phase transformation evolution of lithium iron phosphate with hard X-ray microscopy. *Nature Commun.* **5**, 4570 (2014).
39. Gu, M. *et al.* Conflicting roles of nickel in controlling cathode performance in lithium ion batteries. *Nano Lett.* **12**, 5186–5191 (2012).
40. Zhou, L., Zhao, D. & Lou, X. $\text{LiNi}_{(0.5)}\text{Mn}_{(1.5)}\text{O}_4$ hollow structures as high-performance cathodes for lithium-ion batteries. *Angew. Chem. Int. Ed.* **51**, 239–241 (2012).
41. Petersburg, C. F., Li, Z., Chernova, N. A., Whittingham, M. S. & Alamgir, F. M. Oxygen and transition metal involvement in the charge compensation mechanism of $\text{LiNi}_{1/3}\text{Mn}_{1/3}\text{Co}_{1/3}\text{O}_2$ cathodes. *J. Mater. Chem.* **22**, 19993–20000 (2012).
42. Wilcox, J., Patoux, S. & Doeff, M. Structure and electrochemistry of $\text{LiNi}_{1/3}\text{Co}_{1/3-y}\text{M}_y\text{Mn}_{1/3}\text{O}_2$ (M = Ti, Al, Fe) positive electrode materials. *J. Electrochem. Soc.* **156**, A192–A198 (2009).
43. Kang, S.-H., Yoon, W.-S., Nam, K.-W., Yang, X.-Q. & Abraham, D. P. Investigating the first-cycle irreversibility of lithium metal oxide cathodes for Li batteries. *J. Mater. Sci.* **43**, 4701–4706 (2008).
44. De Groot, F. M. F., Fuggle, J. C., Thole, B. T. & Sawatzky, G. A. 2p x-ray absorption of 3d transition-metal compounds: An atomic multiplet description including the crystal field. *Phys. Rev. B* **42**, 5459–5468 (1990).
45. Lin, F. *et al.* Hole doping in Al-containing nickel oxide materials to improve electrochromic performance. *ACS Appl. Mater. Interfaces* **5**, 301–309 (2013).
46. Lin, F. *et al.* Origin of electrochromism in high-performing nanocomposite nickel oxide. *ACS Appl. Mater. Interfaces* **5**, 3643–3649 (2013).
47. Liu, W. *et al.* Nickel-rich layered lithium transition-metal oxide for high-energy lithium-ion batteries. *Angew. Chem. Int. Ed.* **54**, 4440–4457 (2015).
48. Liu, Y. *et al.* Phase retrieval using polychromatic illumination for transmission X-ray microscopy. *Opt. Express* **19**, 540–545 (2011).
49. Liu, Y. *et al.* TXM-Wizard: A program for advanced data collection and evaluation in full-field transmission X-ray microscopy. *J. Synchrotron Radiat.* **19**, 281–287 (2012).

Acknowledgements

This work was supported by the Assistant Secretary for Energy Efficiency and Renewable Energy, Office of Vehicle Technologies of the US Department of Energy under Contract No. DE-AC02-05CH11231. This research used the Hitachi dedicated STEM of the Center for Functional Nanomaterials, which is a US Department of Energy Office of Science Facility, at Brookhaven National Laboratory under Contract No. DE-SC0012704. The synchrotron X-ray portions of this research were carried out at the Stanford Synchrotron Radiation Lightsource, a Directorate of SLAC National Accelerator Laboratory and an Office of Science User Facility operated for the US Department of Energy Office of Science by Stanford University. Use of the Stanford Synchrotron Radiation Lightsource, SLAC National Accelerator Laboratory, is supported by the US Department of Energy, Office of Science, Office of Basic Energy Sciences under Contract No. DE-AC02-76SF00515. F.L. acknowledges J. Xu and C. Tian for valuable discussion. Y.Liu thanks D. Van Campen for valuable discussions and his engineering support for experiments at beamline 6-2C of SSRL. F.L., D.N. and T.-C.W. would like to thank J.-S. Lee and G. Kerr for their assistance at SSRL. This document was prepared as an account of work sponsored by the United States Government. While this document is believed to contain correct information, neither the United States Government nor any agency thereof, nor the Regents of the University of California, nor any of their employees, makes any warranty, express or implied, or assumes any legal responsibility for the accuracy, completeness, or usefulness of any information, apparatus, product, or process disclosed, or represents that its use would not infringe privately owned rights. Reference herein to any specific commercial product, process, or service by its trade name, trademark, manufacturer, or otherwise, does not necessarily constitute or imply its endorsement, recommendation, or favouring by the United States Government or any agency thereof, or the Regents of the University of California. The views and opinions of authors expressed herein do not necessarily state or reflect those of the United States Government or any agency thereof or the Regents of the University of California.

Author contributions

F.L., Y.Liu, H.L.X. and M.M.D. participated in conceiving and designing the experiments. F.L. performed the materials syntheses, electrochemical measurements and characterization, and wrote the paper with assistance from M.M.D., Y.Liu and H.L.X. F.L., Y.Liu, D.N. and T.-C.W. designed and performed synchrotron experiments. Y.Liu analysed the TXM tomography data. H.L.X. performed STEM-EELS experiments and co-analysed the data with F.L. Y.Li and M.K.Q. participated in developing materials syntheses. L.C. participated in the data analysis and discussion. M.M.D. supervised the project. All authors participated in discussions and know the implications of the work.

Additional information

Supplementary information is available [online](http://www.nature.com/reprints). Reprints and permissions information is available online at www.nature.com/reprints. Correspondence and requests for materials should be addressed to Y.Liu, H.L.X. or M.M.D.

Competing interests

The authors declare no competing financial interests.